

---

**Supplementary information**

---

# **Water cycles in a Hadean CO<sub>2</sub> atmosphere drive the evolution of long DNA**

---

In the format provided by the  
authors and unedited

# Water cycles in a Hadean CO<sub>2</sub> atmosphere drive the evolution of long DNA

Alan Ianeselli<sup>1,2</sup>, Miguel Atienza<sup>1</sup>, Patrick W. Kudella<sup>1,2</sup>, Ulrich Gerland<sup>2,3</sup>, Christof B. Mast<sup>1,2</sup> and Dieter Braun<sup>1,2,\*</sup>

<sup>1</sup>Systems Biophysics, Ludwig Maximilian University Munich, Amalienstraße 54, 80799 München, Germany

<sup>2</sup>Center for NanoScience (CeNS), Ludwig Maximilian University Munich, Amalienstraße 54, 80799 München, Germany

<sup>3</sup>Physics of Complex Biosystems, Technical University of Munich, 85748 Garching, Germany

\*Corresponding author: [dieter.braun@lmu.de](mailto:dieter.braun@lmu.de)

## Content:

1. Simulation of CO<sub>2</sub> absorption into dew and bulk
2. CO<sub>2</sub> dew chamber
3. The dynamics of the RNA-rich dew
4. Setup for FRET and pH measurements
5. RNA hybridization model as a function of pH, salts, length and GC%
6. Finite Element Simulation of DNA accumulation at the heated gas-water interfaces
7. Sequencing of the longer DNA replication products
8. Modeling unspecific replication in the CO<sub>2</sub> dew droplets
9. List of attached files
10. References

## Abbreviations

FRET, Förster Resonance Energy Transfer;  $T_m$ , temperature of melting; pCO<sub>2</sub>, partial pressure of carbon dioxide; FAM, carboxy-fluorescein; ROX, carboxy-rhodamine; RNA, ribonucleic acid; DNA, deoxyribonucleic acid; PAGE, polyacrylamide gel electrophoresis; nt, nucleotides; bp, base pairs; A, adenine; T, thymine; C, cytosine; G, guanine; U, uracil.

## 1. Simulation of CO<sub>2</sub> absorption into dew and bulk

We simulated the dissolution of gaseous carbon dioxide into dew and bulk by solving the differential equations for the carbonate system, as well as the ones for the disodium phosphate buffering system. In our experiments, the concentration of gaseous CO<sub>2</sub> pressure was kept constant. Therefore, also in our simulation it was kept constant over time. Figure S1.1 shows a scheme of the carbonate and phosphate reactions.

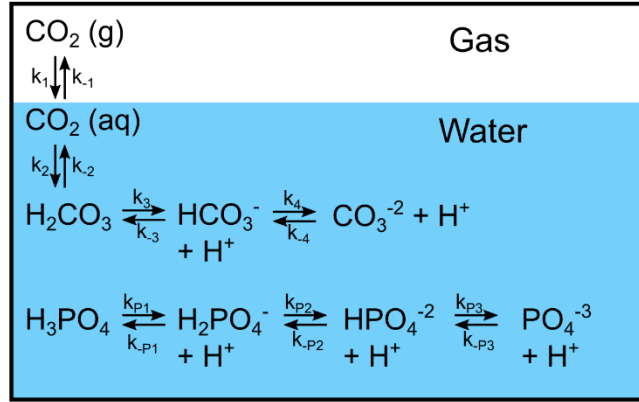


**Figure S1.1: Absorption of CO<sub>2</sub> into water and chemical reactions of the carbonate and phosphate systems.** Schematic representation of the simulated set of chemical reactions that occur when gaseous CO<sub>2</sub> is dissolved into an aqueous solution containing phosphate buffer. After its dissolution into water, the formation of the different carbonate species also releases protons. The phosphate species are a buffering system.

$$\frac{d[CO_2(g)]}{dt} = 0 \quad (1)$$

$$\frac{d[CO_2(aq)]}{dt} = k_1[CO_2(g)] - k_{-1}[CO_2(aq)] - k_2[CO_2(aq)] + k_{-2}[H_2CO_3] \quad (2)$$

$$\frac{d[H_2CO_3]}{dt} = k_2[CO_2(aq)] - k_{-2}[H_2CO_3] - k_3[H_2CO_3] + k_{-3}[H^+][HCO_3^-] \quad (3)$$

$$\begin{aligned} \frac{d[H^+]}{dt} = & k_3[H_2CO_3] - k_{-3}[H^+][HCO_3^-] + k_4[HCO_3^-] - k_{-4}[H^+][CO_3^{2-}] + k_{P1}[H_3PO_4] + k_{P2}[H_2PO_4^-] + k_{P3}[HPO_4^{2-}] \\ & - k_{-P1}[H_2PO_4^-][H^+] - k_{-P2}[HPO_4^{2-}][H^+] - k_{-P3}[PO_4^{3-}][H^+] \end{aligned} \quad (4)$$

$$\frac{d[HCO_3^-]}{dt} = k_3[H_2CO_3] - k_{-3}[H^+][HCO_3^-] - k_4[HCO_3^-] + k_{-4}[H^+][CO_3^{2-}] \quad (5)$$

$$\frac{d[CO_3^{2-}]}{dt} = k_4[HCO_3^-] - k_{-4}[H^+][CO_3^{2-}] \quad (6)$$

$$\frac{d[H_3PO_4]}{dt} = k_{-P1}[H_2PO_4^-][H^+] - k_{P1}[H_3PO_4] \quad (7)$$

$$\frac{d[H_2PO_4^-]}{dt} = k_{-P2}[HPO_4^{2-}][H^+] - k_{P2}[H_2PO_4^-] + k_{P1}[H_3PO_4] - k_{-P1}[H_2PO_4^-][H^+] \quad (8)$$

$$\frac{d[HPO_4^{2-}]}{dt} = k_{-P3}[PO_4^{3-}][H^+] - k_{P3}[HPO_4^{2-}] - k_{-P2}[HPO_4^{2-}][H^+] + k_{P2}[H_2PO_4^-] \quad (9)$$

$$\frac{d[PO_4^{3-}]}{dt} = k_{P3}[HPO_4^{2-}] - k_{-P3}[PO_4^{3-}][H^+] \quad (10)$$

The differential equations shown above (1 – 10) were solved using the software COMSOL Multiphysics, using the rates and parameters indicated in table S1.1.

Parameter	Value	Description	Source
k <sub>1</sub>	1 · 10 <sup>-2</sup> [s <sup>-1</sup> ]	CO <sub>2</sub> (g) → CO <sub>2</sub> (aq)	Al-Hindi & Azizi <sup>1</sup>
k <sub>-1</sub>	12 · 10 <sup>-3</sup> [s <sup>-1</sup> ]	CO <sub>2</sub> (aq) → CO <sub>2</sub> (g)	
k <sub>2</sub>	6 · 10 <sup>-2</sup> [s <sup>-1</sup> ]	CO <sub>2</sub> (aq) → H <sub>2</sub> CO <sub>3</sub>	Bond <i>et al.</i> <sup>2</sup>
k <sub>-2</sub>	2 · 10 <sup>1</sup> [s <sup>-1</sup> ]	H <sub>2</sub> CO <sub>3</sub> → CO <sub>2</sub> (aq)	Pocker & Bjorkquist <sup>3</sup>
k <sub>3</sub>	1 · 10 <sup>7</sup> [s <sup>-1</sup> ]	H <sub>2</sub> CO <sub>3</sub> → HCO <sub>3</sub> <sup>-</sup> + H <sup>+</sup>	
k <sub>-3</sub>	5 · 10 <sup>10</sup> [M <sup>-1</sup> s <sup>-1</sup> ]	H <sup>+</sup> + HCO <sub>3</sub> <sup>-</sup> → H <sub>2</sub> CO <sub>3</sub>	Warneck <sup>4</sup>
k <sub>4</sub>	3 · 10 <sup>0</sup> [s <sup>-1</sup> ]	HCO <sub>3</sub> <sup>-</sup> → CO <sub>3</sub> <sup>2-</sup> + H <sup>+</sup>	
k <sub>-4</sub>	5 · 10 <sup>10</sup> [M <sup>-1</sup> s <sup>-1</sup> ]	CO <sub>3</sub> <sup>2-</sup> + H <sup>+</sup> → HCO <sub>3</sub> <sup>-</sup>	Keil <i>et al.</i> <sup>5</sup>
k <sub>P1</sub>	k <sub>-P1</sub> · 10 <sup>-pK<sub>1</sub></sup> [s <sup>-1</sup> ]	H <sub>3</sub> PO <sub>4</sub> → H <sub>2</sub> PO <sub>4</sub> <sup>-</sup> + H <sup>+</sup>	
k <sub>-P1</sub>	10 <sup>13</sup> [M <sup>-1</sup> s <sup>-1</sup> ]	H <sub>2</sub> PO <sub>4</sub> <sup>-</sup> + H <sup>+</sup> → H <sub>3</sub> PO <sub>4</sub>	
k <sub>P2</sub>	k <sub>-P2</sub> · 10 <sup>-pK<sub>2</sub></sup> [s <sup>-1</sup> ]	H <sub>2</sub> PO <sub>4</sub> <sup>-</sup> → HPO <sub>4</sub> <sup>2-</sup> + H <sup>+</sup>	
k <sub>-P2</sub>	10 <sup>13</sup> [M <sup>-1</sup> s <sup>-1</sup> ]	HPO <sub>4</sub> <sup>2-</sup> + H <sup>+</sup> → H <sub>2</sub> PO <sub>4</sub> <sup>-</sup>	
k <sub>P3</sub>	k <sub>-P3</sub> · 10 <sup>-pK<sub>3</sub></sup> [s <sup>-1</sup> ]	HPO <sub>4</sub> <sup>2-</sup> → PO <sub>4</sub> <sup>3-</sup> + H <sup>+</sup>	
k <sub>-P3</sub>	10 <sup>13</sup> [M <sup>-1</sup> s <sup>-1</sup> ]	PO <sub>4</sub> <sup>3-</sup> + H <sup>+</sup> → HPO <sub>4</sub> <sup>2-</sup>	
pK <sub>1</sub>	2.12	1st dissociation constant	
pK <sub>2</sub>	7.21	2st dissociation constant	
pK <sub>3</sub>	12.67	3st dissociation constant	

**Table S1.1: Parameters for the carbonate and phosphate chemical reactions.**

Initial concentrations are reported in table S1.2.

Species	Initial concentrations
CO <sub>2</sub> (g)	1.43 · 10 <sup>-5</sup> [M] (ambient pCO <sub>2</sub> = 4 · 10 <sup>-4</sup> bar)
CO <sub>2</sub> (aq)	1.17 · 10 <sup>-5</sup> [M]
H <sub>2</sub> CO <sub>3</sub>	3.52 · 10 <sup>-8</sup> [M]
HCO <sub>3</sub> <sup>-</sup>	2.61 · 10 <sup>-6</sup> [M]
CO <sub>3</sub> <sup>2-</sup>	5.82 · 10 <sup>-11</sup> [M]
H <sup>+</sup>	2.69 · 10 <sup>-6</sup> [M] (pH = 5.6)

**Table S1.2: Initial carbonate concentrations after equilibration at room pCO<sub>2</sub>.** The concentration for each species (left column) is reported in the right column.

The following table contains the formulas to calculate the initial concentration of the phosphate species. The total phosphate concentration was 10 mM for the bulk and 0 mM for the dew.

Species	Initial concentrations
H <sub>3</sub> PO <sub>4</sub>	$[\text{H}_2\text{PO}_4^-] \cdot 10^{(-\text{pH}+\text{p}K_1)}$ [M]
H <sub>2</sub> PO <sub>4</sub> <sup>-</sup>	$[\text{HPO}_4^{2-}] \cdot 10^{(-\text{pH}+\text{p}K_2)}$ [M]
HPO <sub>4</sub> <sup>2-</sup>	$[\text{PO}_4^{3-}] \cdot 10^{(-\text{pH}+\text{p}K_3)}$ [M]
PO <sub>4</sub> <sup>3-</sup>	$\frac{c_0}{(1+10^{(-\text{pH}+\text{p}K_3)})}$ [M]
c <sub>0</sub>	0.01 (bulk) or 0 (dew) [M]

**Table S1.3: Initial concentrations of the phosphate species.** The formula for each species (left column) is reported in the right column.

The following Figure S1.2 shows an example of CO<sub>2</sub> acidification into the dew (total phosphate concentration 0 M). At an arbitrary time, the partial pressure of carbon dioxide was increased from ambient (0.4 mbar) to 1 bar, and then decreased to ambient again after the necessary equilibration time. The data that were obtained are consistent, both in terms of timescale and value, with experiments of carbon dioxide absorption and desorption<sup>1</sup> and equilibrium calculations based on equilibrium constants<sup>6,7</sup>. With a pH-sensitive fluorescent dye (Lysosensor Yellow/Blue DND-160), the pH change of pure water was measured experimentally. The data are shown in Figure S1.2a and clearly show the same behavior of the model. The slight positive slope of the experimental data is due to photo-bleaching of the Lysosensor fluorophore over time. To better visualize the data, we created the Bjerrum plot of our carbonate system model (Figure S1.3).

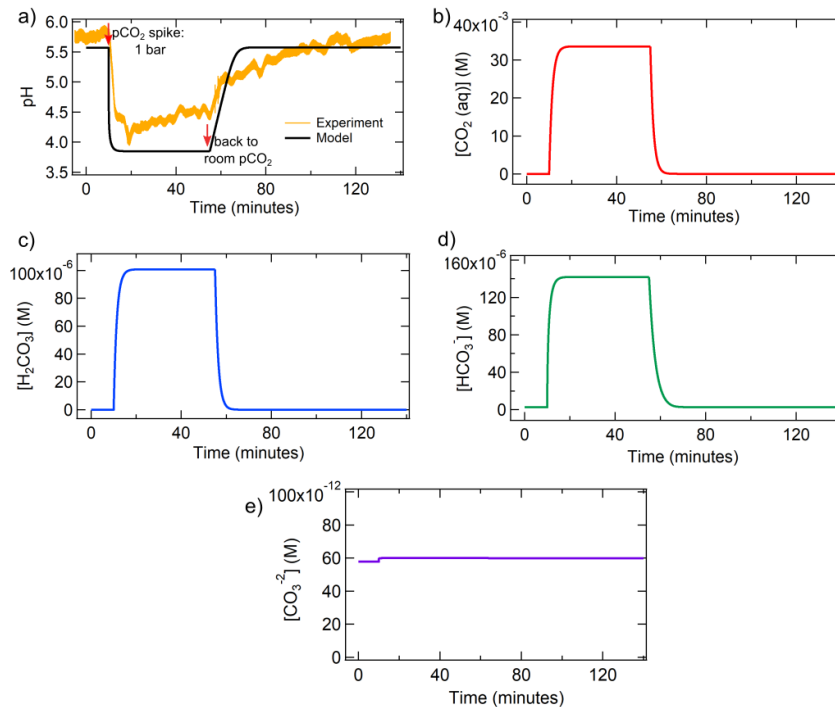


**Figure S1.2: Kinetics of pH and carbonate in the dew after a CO<sub>2</sub> spike.** pH (a), dissolved CO<sub>2</sub> (b), H<sub>2</sub>CO<sub>3</sub> (c), HCO<sub>3</sub><sup>-</sup> (d) and CO<sub>3</sub><sup>2-</sup> (e) over time. The red arrows shown in a) indicate the moments of pCO<sub>2</sub> change: from ambient CO<sub>2</sub> to 1 bar (first arrow) and vice versa (second arrow), respectively.

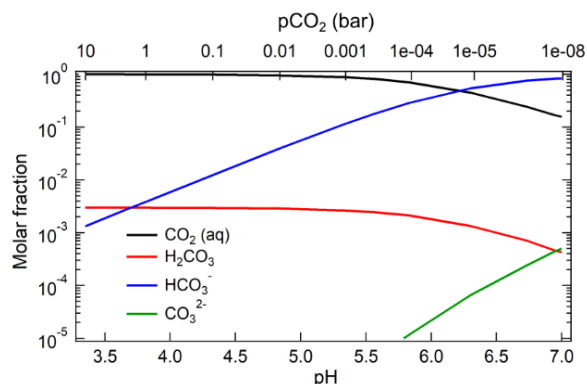


**Figure S1.3: Simulated Bjerrum plot in the dew.** a) Bjerrum plot: molar fraction of the carbonate species as a function of pH at steady state (assumed to be steady after 600 seconds of simulation). CO<sub>2</sub> partial pressures in the range from 10  $\mu$ bar to 10 bar yielded a pH range from 7.0 to 3.3.

## 2. CO<sub>2</sub> dew chamber

Our reaction chamber (aka “dew chamber”) consisted of a thin chamber (14 mm x 30 mm x 250  $\mu$ m) made of Teflon, placed between a transparent sapphire window and a silicon back plate (the latter was covered with a thin Teflon foil). To establish a temperature gradient, we differentially heated the sapphire with rod resistors and the silicon plate with a Peltier element. The sapphire window included four holes, where microfluidic tubings were attached (see tubing numbers in Figure S2), in order to control the sample inflow and outflow to the chamber, to insert gaseous carbon dioxide and to measure the inner barometric pressure.

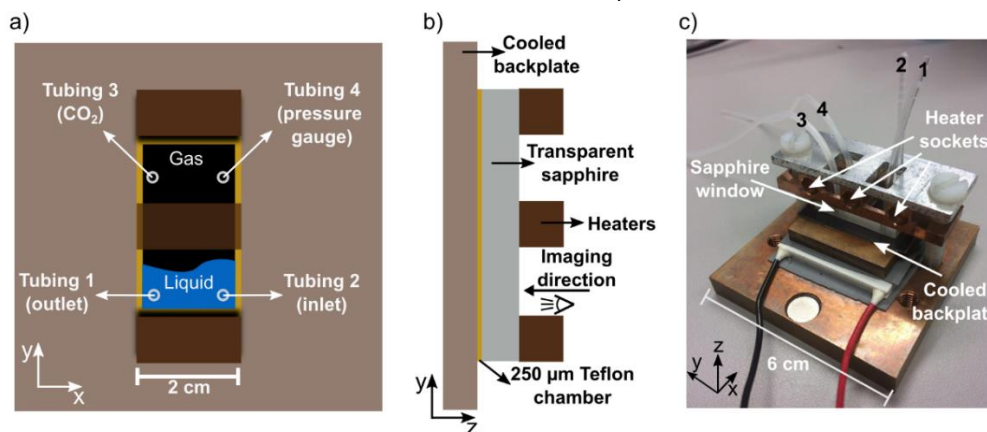


**Figure S2. Scheme and photo of our microfluidic dew chamber.** a) Front scheme of the chamber. b) Lateral scheme of the dew chamber. c) Photo of the dew chamber. The Peltier element can be seen below the back plate. Heaters (rod resistors) are inserted into the three heater sockets at the top of the chamber.

To produce a high pressure CO<sub>2</sub> atmosphere, we exploited the expansion properties of solid CO<sub>2</sub> upon sublimation. When dry ice changes its state from solid to gas, its volume increases about a factor of  $\sim$ 800. A bottle containing approximately 20 g of dry ice was connected to one of the tubings of our dew chamber. A handmade pressure regulator was connected to the bottle, which controlled an external vent and therefore the CO<sub>2</sub> flux inside the dew chamber. Upon sublimation, the 20 g of dry ice transformed into a volume of  $\sim$ 11 liters of gaseous carbon dioxide in a time span of approximately 30 minutes. The pressure was held constant to the final value, with an estimated accuracy of  $\pm$  0.05 bar. For the replication experiments, which required a carbon dioxide supply for several hours, the CO<sub>2</sub> gas was delivered using pressurized CO<sub>2</sub>-containing flasks.

### 3. The dynamics of the RNA-rich dew

As already discussed in the main manuscript, the moving gas-water interface left RNA in the dry state on the warm sapphire, as a consequence of the so-called coffee-ring effect<sup>8</sup>. Fluorescent RNA in the dry state had a low quantum yield, and this was the reason why it could not be easily seen by fluorescence. When a droplet of dew, which nucleated on the cold side, became thicker than 250  $\mu\text{m}$  (the thickness of our chamber) it touched the opposite warm sapphire, where the fluorescent RNA in the dry state was present. Therefore, it could re-dissolve RNA and become fluorescent again, as the quantum yield of the fluorophore increased. To get a deeper understanding of the droplet dynamics, we imaged our microfluidic dew chamber using a combination of bright field and fluorescence microscopy. The blue LED excited the FAM-labeled RNA, while a lamp homogeneously illuminated the chamber. The intensities of the light sources were adjusted in such a way to discriminate between the non-fluorescent, pure water dew on the cold side (that could be seen as dim shiny spheres) and the fluorescent dew, that re-dissolved the dry RNA on the warm side (which appeared very bright).

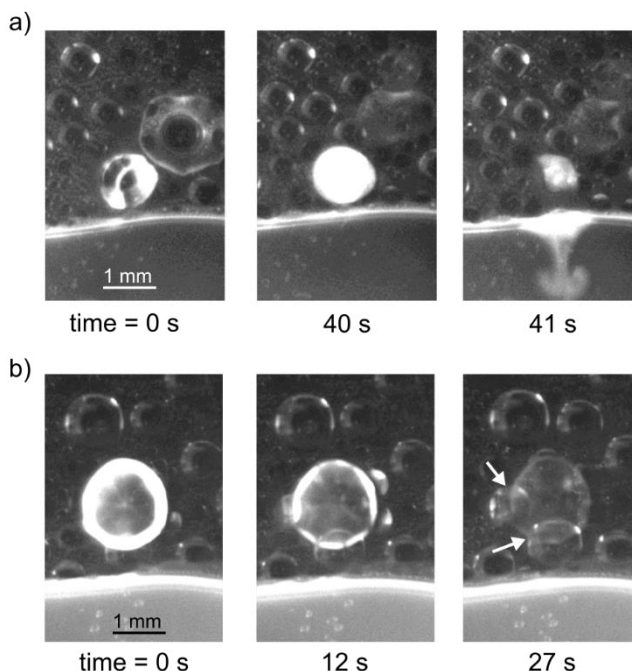


**Figure S3: The two possible fates of a dew droplet.** a) Growth and coalescence. The coalescence event could be seen by the fluorescent trace of the RNA left in the bulk (right picture). b) Evaporation and “jump” on the hot wall. The jump was confirmed by novel dew droplets of pure water that could be seen growing behind (indicated by the white arrows). Here, experimental conditions were the following: 250  $\mu\text{m}$  (a) and 500  $\mu\text{m}$  (b) chamber thickness, temperature gradient of 24  $^{\circ}\text{C}$  (cold side 15  $^{\circ}\text{C}$ , warm side 39  $^{\circ}\text{C}$ ), and ambient  $\text{CO}_2$  pressure. The solution consisted of 5  $\mu\text{M}$  RNA (single stranded), 12.5 mM  $\text{MgCl}_2$ , 10 mM TRIS, pH 7.0.

A RNA-containing dew droplet could have two different fates:

- (i) Growth and coalescence with the bulk. When other dew droplets grew in the proximity of the droplet of interest, they fused together. The size of the dew droplet increased, up to a point where it fell down or touched the bulk and coalesced with it. This transported the dissolved RNA back into the bulk solution. The dew droplets were the site of RNA denaturation. Therefore, the “coalescence fate” would periodically provide the reshuffling of RNA strands to the bulk solution where the replication reaction then could take place. The mechanism is shown in Figure S3a.
- (ii) Evaporation and drying. As just discussed, when a dew droplet on the cold wall grew enough, it hit the warm sapphire. Due to the higher temperature of the sapphire, the dew droplet slowly started to evaporate, and RNA dried again. Initially, the droplet touched both the warm and cold sides (as a capillary bridge), and then eventually “jumped” on the sapphire. The dry fluorophore had a lower quantum yield. This made the RNA fluorescent signal disappear as the droplet evaporated. The mechanism is shown in Figure S3b. This mechanism was an efficient source of wet-dry cycles which were responsible for the unspecific polymerization reactions that we observed in our system.

#### 4. Setup for FRET and pH measurements

To quantify the fraction of duplex RNA, we applied an alternating illumination protocol<sup>9,10</sup>. The two RNA strands were differentially labeled with FAM (Carboxy-fluorescein) and ROX (Carboxy-Rhodamine): a FRET pair. The first LED (blue) excited the donor (FAM) directly and the acceptor (ROX) could be excited only if the two dyes were within the FRET range. The second LED (amber) excited the acceptor only. The spatially-averaged, temperature-dependent, crosstalk- and artifact-corrected FRET signal was calculated as following<sup>11</sup>:

$$FRET(T) = \frac{DA(T) \cdot da(pCO_2) - dd(T) \cdot DD(T) - aa(T) \cdot AA(T)}{AA(T) \cdot aa(pCO_2)} \quad (11)$$

where  $aa(T)$ ,  $dd(T)$ ,  $da(CO_2)$  and  $aa(CO_2)$  corrected for non-FRET artifact signals in the DA and AA channels and were defined as:

$$dd(T) = \frac{DA_D(T)}{DD_D(T)} \quad aa(T) = \frac{DA_A(T)}{AA_A(T)} \quad (12, 13)$$

$$da(pCO_2) = \frac{DA_D(pCO_2)}{DA_D(pCO_2^{ref})} \quad aa(pCO_2) = \frac{DA_A(pCO_2)}{AA_A(pCO_2^{ref})} \quad (14, 15)$$

where  $T$  refers to temperature,  $pCO_2$  to the partial pressure of  $CO_2$  and  $pCO_2^{ref}$  indicates the reference  $pCO_2$  condition (room  $pCO_2$ ). Results are shown in Figure S4.1. All channels were defined according to table S4.

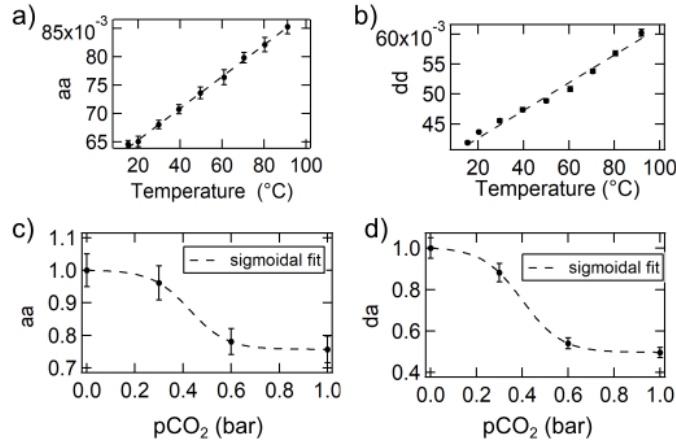


**Figure S4.1: Correction of non-FRET artifacts.** a-b) Crosstalk between the donor and acceptor channels calculated as a function of temperature and linearly fitted. c-d) Correction of  $CO_2$ -related artifacts in the range between 0 and 1 bar  $pCO_2$ .

Prior to every experiment, a melting curve in the bulk and at ambient  $pCO_2$  was measured, in order to calculate the coefficients  $\alpha = \min(FRET(T))$  and  $\beta = \max(FRET(T)) - \alpha$  and normalize the FRET signal between 1 and 0:

$$FRET(T) = \frac{FRET(T) - \alpha}{\beta} \quad (16)$$



Channel	Excitation	Emission	Labelling
<i>DA</i>	FAM 470 nm	ROX 630 nm	FAM, ROX
<i>DD</i>	FAM 470 nm	FAM 536 nm	FAM, ROX
<i>AA</i>	ROX 590 nm	ROX 630 nm	FAM, ROX
<i>AA<sub>A</sub></i>	ROX 590 nm	ROX 630 nm	ROX
<i>DD<sub>D</sub></i>	FAM 470 nm	FAM 536 nm	FAM
<i>DA<sub>D</sub></i>	FAM 470 nm	ROX 630 nm	FAM
<i>DA<sub>A</sub></i>	FAM 470 nm	ROX 630 nm	ROX

**Table S4: Definition of the channels for FRET calculation.** The letters denote the excitation or emission wavelength. The index indicates which dyes are used (no index = both dyes are used). D = Donor (FAM), A = Acceptor (ROX).

We used the pH-sensitive ratiometric dye Lysosensor Yellow/Blue DND-160 to calculate the pH of the bulk and dew. From a stock concentration of 1 mM in DMSO, Lysosensor was diluted to a final concentration of 20  $\mu$ M in aqueous solution. Through a modified Henderson-Hasselbach equation, the ratio  $R$  between the Lysosensor emission maximum at 540 nm upon alternating excitation at  $\lambda_1 = 329$  nm and  $\lambda_2 = 384$  nm was modeled by the following equation<sup>12</sup>:

$$pH = a + b \cdot \log\left(\frac{R - R_a}{R_b - R}\right) \quad (17)$$

where  $a$  denotes the pKa of Lysosensor,  $b$  accounts for the weighting of the emission spectra,  $R$  is defined as the ratio between fluorescence (F) emission at 540 nm upon excitation at  $\lambda_1$  or  $\lambda_2$  ( $R = F_{\lambda_1}/F_{\lambda_2}$ ), and  $R_a$  and  $R_b$  account for the maximum and minimum fluorescence ratios, respectively. To correct for temperature-dependent shifts of the pH calibration curve, the parameters  $a$ ,  $b$ ,  $R_a$  and  $R_b$  have been fitted linearly in function of temperature, as shown in Figure S4.2. The calibration has been made in 10 mM Na<sup>+</sup>-citrate buffer at various pH (range 1.6 to 7), using Lysosensor at a concentration of 20  $\mu$ M. 10 mM MgCl<sub>2</sub> were also added. Solutions with different pH have been created by ratiometrically mixing different amounts of powders of citric acid and sodium citrate dihydrate. Final pH has been adjusted by dripping HCl or NaOH.

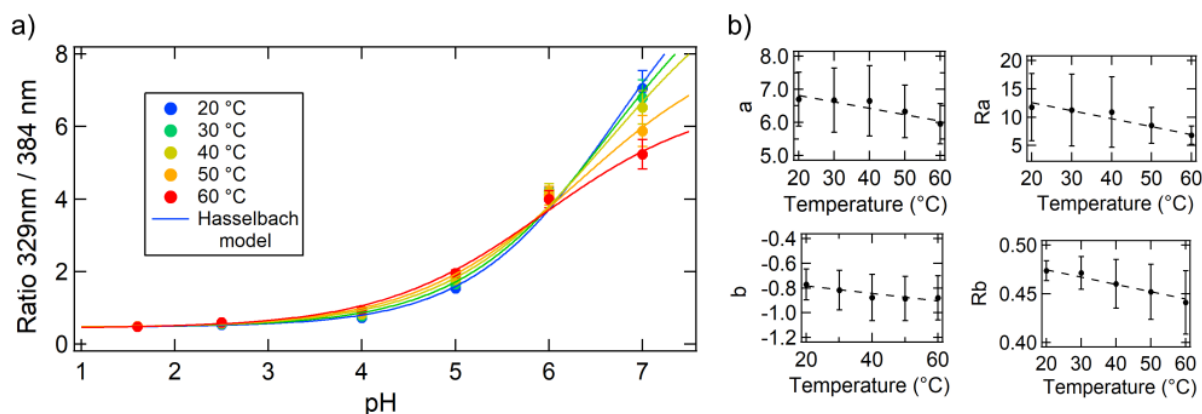


**Figure S4.2: pH calibration curve of Lysosensor Yellow/Blue DND-160.** a) Fluorescence ratio  $R$  measured between pH 1.6 - 7.0 and at different temperatures. The data have been fitted with the modified Handerson-Hasselbach equation (equation 17). b) The parameters  $a$ ,  $b$ ,  $Ra$  and  $Rb$  have been linearly fitted to adjust the temperature shifts of the Ratio to pH curve. Error bars in (a) indicate the standard deviation from experimental measurements ( $n \sim 10$ ). Error bars in (b) indicate the standard deviation of the fit parameters.

The setup for FRET and pH consisted of a handmade standard fluorescence microscope (Zeiss Axiotech Vario microscope body) equipped with four excitation LEDs (M340L4, M385L2, M470L2, M590L2, from Thorlabs), excitation filters (BP 340/26, BP 379/34, BP 482/35, BP 588/20), beamsplitters (DC 475/40, DC 425 LP, DC 365 LP), a triple-edge dichroic mirror (DC 395/495/610), an Optosplit II with a ratiometric filter set (DC 600 LP, BP 536/40, BP 630/50), a Stingray-F145B ASG camera (ALLIED Vision Technologies GmbH) and a 1X objective (AC254-100-A-ML Achromatic Doublet). The former specifications regarding LEDs, filters, beamsplitters and dichroic mirrors were given in nanometers. The software LabVIEW was used to control the microscope's electronics. A scheme of the setup is given in the following Figure S4.3:

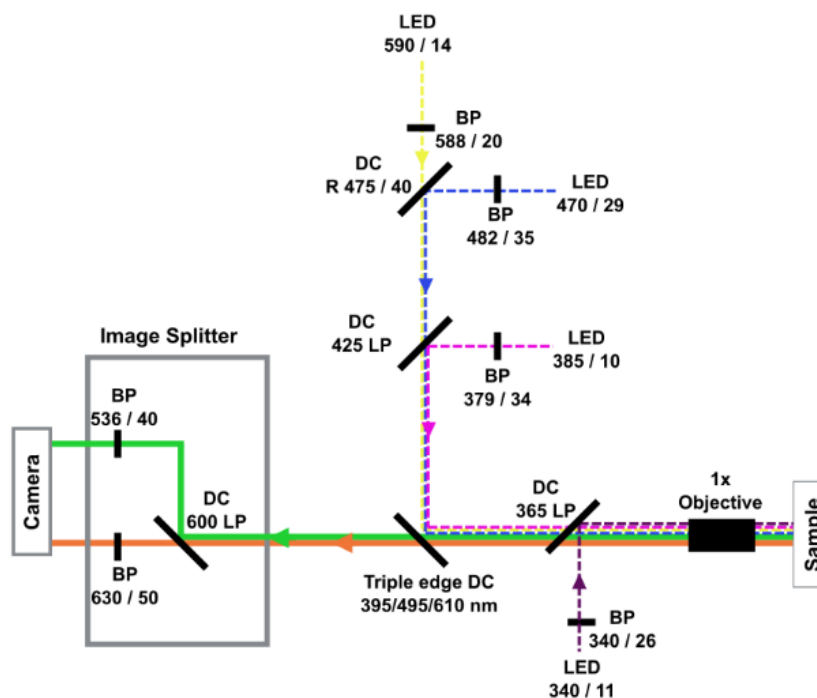


**Figure S4.3: Scheme of the setup for FRET and pH measurements.** Four alternating LEDs have been used to excite FAM (blue LED), ROX (amber LED), and the two excitation maxima of Lysosensor (340 nm and 385 nm LEDs). Each LED was alternatively switched on for 100 ms. Therefore, the camera recorded four images per cycle. Together with the dead times, the camera frame rate was approximately 8 fps.

## 5. RNA hybridization model as a function of pH, salts, length and GC%

The stability of duplex oligonucleotides (RNA or DNA) in solution is determined by many factors. Intrinsic properties like sequence length and sequence composition play a crucial role, as well as environmental factors such as pH<sup>13</sup> and the concentration of ions<sup>10</sup> in solution. We modeled hybridization creating a model based on van 't Hoff to calculate the melting curve of RNA as a function of pH, Mg<sup>2+</sup> concentration, sequence length and the GC content of the sequence. The van 't Hoff equation is the following:

$$\ln K_{eq} = -\frac{\Delta H}{RT} + \frac{\Delta S}{R} \quad (18)$$

where  $K_{eq}$  is the annealing equilibrium constant,  $\Delta H$  and  $\Delta S$  are the standard enthalpy and entropy changes,  $T$  is the temperature and  $R$  is the gas constant. The model has been calibrated on experimental melting curves measured by FRET. Given the melting curve for every specific condition (pH, Mg<sup>2+</sup>, GC% and sequence length) the data have been converted in the form of equation 18 (van 't Hoff), and then fitted with a linear function to obtain  $\Delta H/R$  and  $\Delta S/R$ . In order to calculate  $\Delta H/R$  and  $\Delta S/R$  in function of pH, Mg<sup>2+</sup>, GC% and sequence length, only one parameter at a time has been changed, while the others remained constant. For what concerns pH and Mg<sup>2+</sup>,  $\Delta H/R$  and  $\Delta S/R$  have been fitted with a power law, a linear fit was used in the cases of GC% and an exponential fit for sequence length. The results are shown in Figure S5.1.

The linear fits of the van 't Hoff plots shown in Figure S5.1 are based on the assumption that entropy and enthalpy are constant over temperature changes. This assumption is not always correct, but the predictions of the model resulted to be adequately accurate for many sequences of different lengths and composition, and for a large range of pH and MgCl<sub>2</sub> values, as shown in Figure S5.2. Therefore, the assumption of linearity is a good approximation for the type of calculations that we considered.

Given the enthalpic and entropic terms calculated and fitted as previously explained, it was then possible to calculate the equilibrium constant for each parameter at a given temperature. To obtain the final equilibrium constant of the model ( $K_{eq}^{total}$ ), the individual enthalpies and entropies for each parameter have been put together to calculate the total enthalpy and the total entropy as following:

$$\Delta H_{total} = \frac{\Delta H(pH)}{\Delta H(pH_{ref})} \cdot \frac{\Delta H(Mg^{2+})}{\Delta H(Mg_{ref}^{2+})} \cdot \frac{\Delta H(length)}{\Delta H(length_{ref})} \cdot \frac{\Delta H(GC\%)}{\Delta H(GC\%_{ref})} \cdot \Delta H_{ref} \quad (19)$$

$$\Delta S_{total} = \frac{\Delta S(pH)}{\Delta S(pH_{ref})} \cdot \frac{\Delta S(Mg^{2+})}{\Delta S(Mg_{ref}^{2+})} \cdot \frac{\Delta S(length)}{\Delta S(length_{ref})} \cdot \frac{\Delta S(GC\%)}{\Delta S(GC\%_{ref})} \cdot \Delta S_{ref} \quad (20)$$

$$\ln K_{eq}^{total} = -\frac{\Delta H_{total}}{RT} + \frac{\Delta S_{total}}{R} \quad (21)$$

where  $\Delta H_{ref}$  and  $\Delta S_{ref}$  correspond to the reference enthalpy and entropy at the arbitrary reference condition of pH, Mg<sup>2+</sup>, length and GC%. This means that the enthalpy and entropy of the (arbitrary) reference condition are multiplied by a factor between 0 and  $+\infty$ , and the final equilibrium constant is calculated according to equation (21) (van 't Hoff equation).

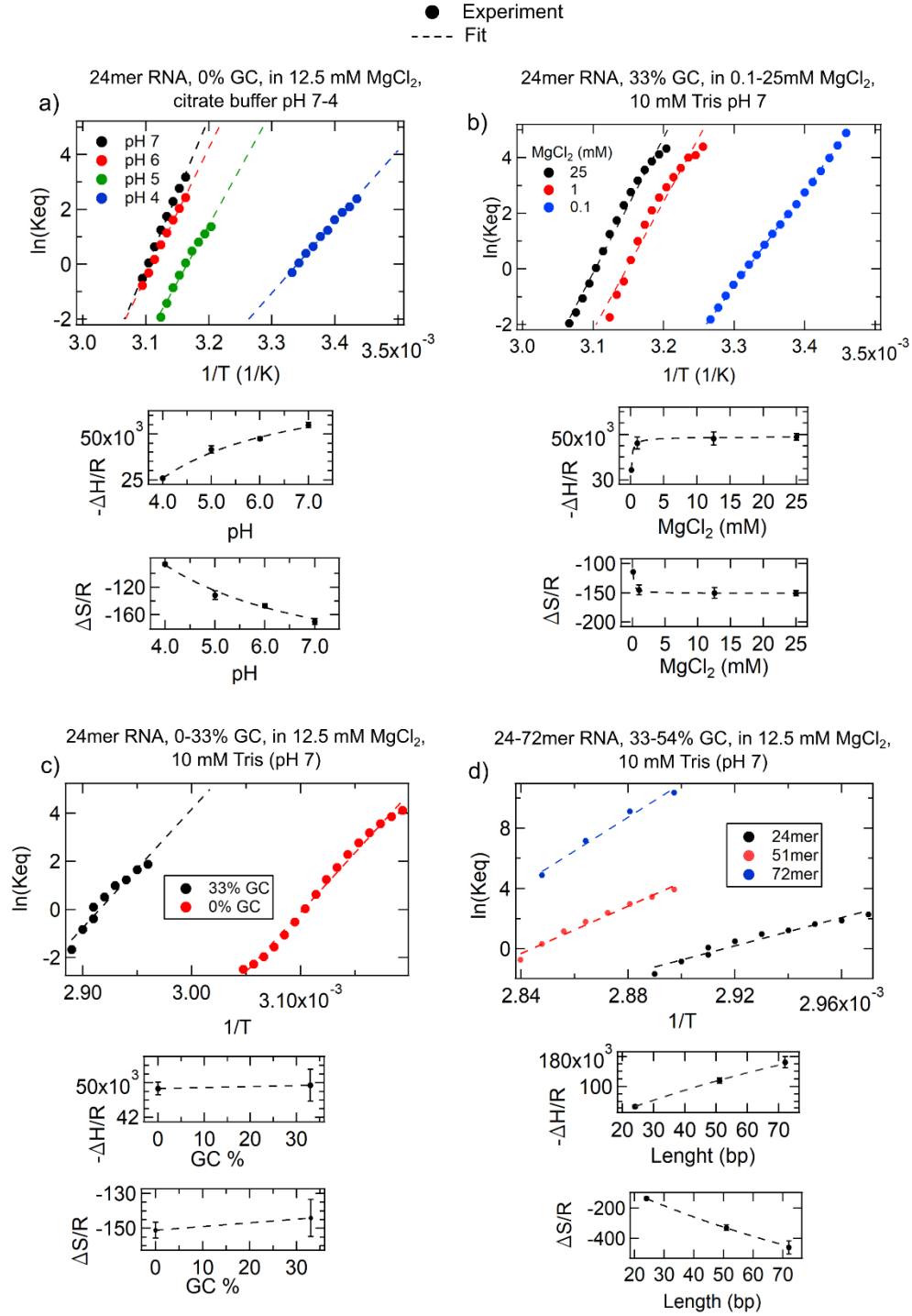


**Figure S5.1: Experimental van 't Hoff plots used for the calibration of the model.** RNA melting curves at different pH (a),  $Mg^{2+}$  (b), GC % (c) and sequence length (d), in the form of equation (18) (large plots), have been used to calculate enthalpy and entropy in function of the respective parameter (small plots).  $\Delta H/R$  and  $\Delta S/R$  have then been fitted with a power law (a and b), linearly (c) or with an exponential function(d).

With minimal discrepancies, the model successfully re-predicted the melting curves it was calibrated with, indicating that the method that we developed to put together the enthalpies and entropies is successful. Results are shown in Figure S5.2.

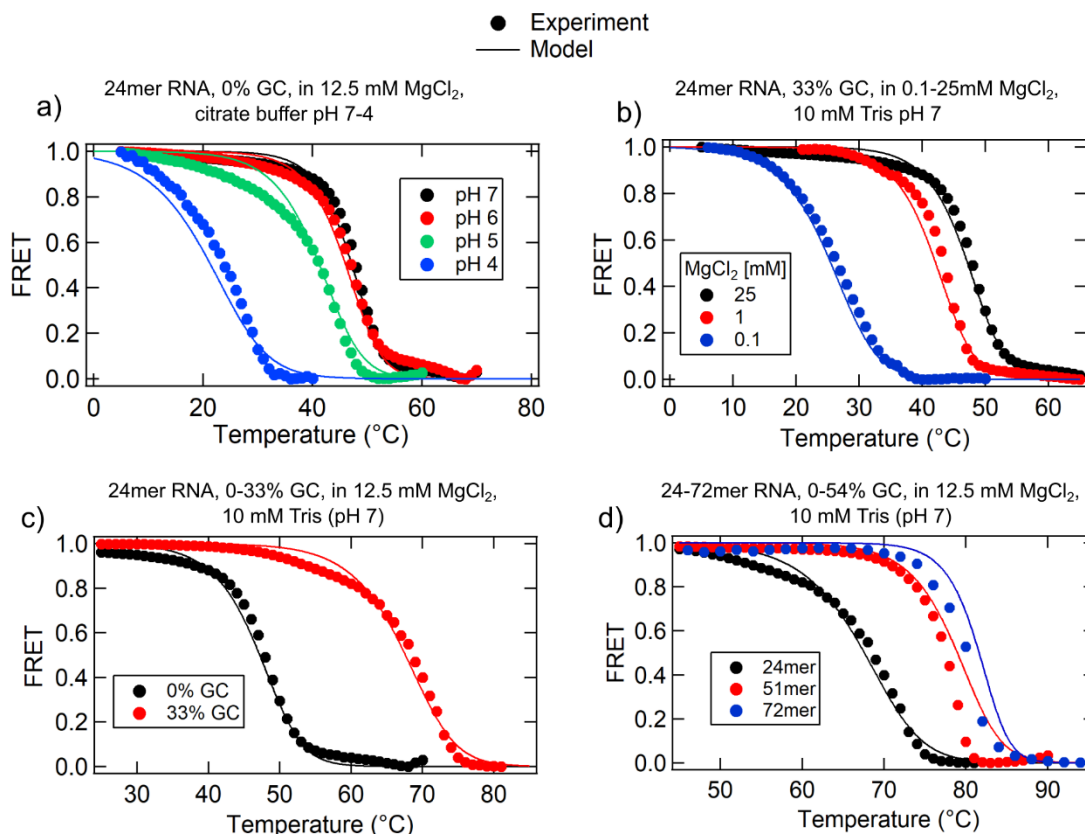


**Figure S5.2: Experimental vs simulated melting curves.** The experimental melting curves (points) at different pH (a),  $Mg^{2+}$  (b), GC % (c) and sequence length (d) have been compared to the melting curves calculated with our model (continuous lines). With only minor deviations, the experiment and the model show good agreement both in terms of the shape of the curve and the resulting melting temperature

The model described here has been used to obtain the data shown in Figure 2, e and Figure 5. By comparison with experimental data, it allowed us to determine the average salt concentration within the dew droplets, which resulted to be in the order of 0.25 mM  $MgCl_2$ .

This model helped us to better understand how the hybridization of oligonucleotides worked in a system of pH and salt fluctuations, where a water cycle at high  $pCO_2$  continuously oscillated RNA between low-salt acidic dew droplets, and a pH-neutral salt-rich bulk. As already shown in Figure 2e and in the next Figure S5.3, the conditions of the bulk lied within a flatland region where the duplex oligo form is stable (this can be seen as a white/cyan surface (high  $T_m$ ) in Figure S5.3, or as a yellow one (high FRET) in Figure 2e). On the other hand, the dew droplets lied outside of that flatland, after a circular boundary with a sudden drop in  $T_m$  and FRET. There, the duplex form became unstable. It is interesting to see that the shape of that boundary is not a square, but is rather circular. This indicates that the destabilizing effects of low pH and low salt concentration act synergistically.

The model is given in the supplementary file "[melting\\_curve\\_calculator.exe](#)"

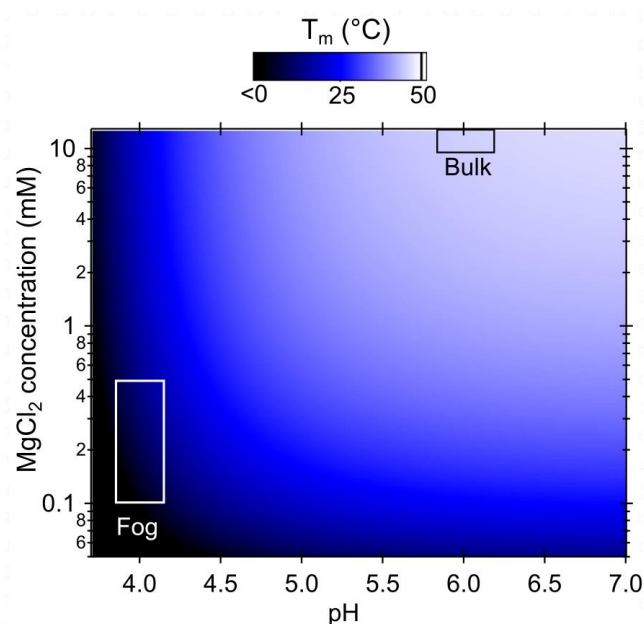


**Figure S5.3: Surface plot of the simulated melting temperature.** The surface plot shows how the melting temperature of a 24bp RNA, 0% GC varies as a function of pH and  $Mg^{2+}$ . The boxes inside of the plot indicate the existence regime of the bulk and of the dew droplets, when the gas contains 1 bar of  $pCO_2$ . This plot complements to the one shown in Figure 2e.

Using the hybridization model developed here, we could determine the stability of DNA or RNA in the bulk and dew as a function of pH. This helped us in estimating the pH range in which the dew and bulk maintain their denaturing and annealing characteristics, respectively. The concentration of  $Mg^{2+}$  is fixed at 0.25 mM in the dew and at 10 mM in the bulk. Results are shown in Figure S5.4, calculated in the conditions for the experiments shown in Figure 2d, 4a-c and 4d.

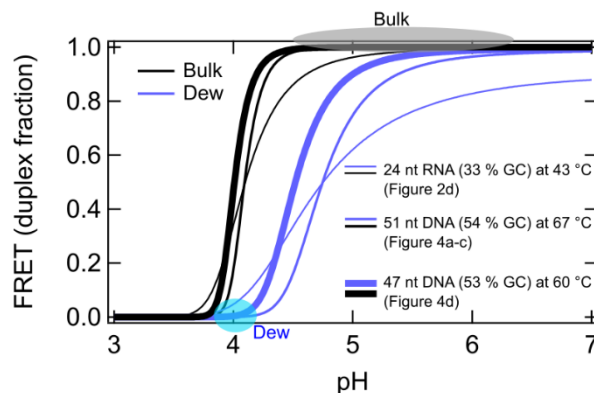


**Figure S5.4: Duplex fraction as a function of pH in the dew and bulk.** We calculated the duplex fraction of oligonucleotides for three different conditions: 24 nt RNA 33 % GC at 43 °C (thin lines), 51 nt DNA 54 % GC at 67 °C (medium lines), 47 nt DNA 53 % GC at 60 °C (thick lines), which correspond to the conditions of the experiments shown in Figure 2d, 4a-c and 4d, respectively. The colored circles generally indicate the expected pH of the dew (cyan circle) and bulk (gray ellipse) after  $CO_2$  acidification. The bulk and the dew are micro habitats that have opposite effects on DNA stability, and can perform their functions also at higher temperatures.

Up to 67 °C, the dew always maintained denaturing conditions ( $FRET < 0.2$ ) for pH up to  $\sim 4.2$ . The pH of low-salt water (i.e. dew) at 1 bar  $pCO_2$  is supposed to remain below 4.0 for temperatures up to 80 °C<sup>14</sup>. Therefore, in the dew, the denaturation of the oligonucleotides that we used in our experiments was certain, and the assumption of a dew's pH of 4 for the calculations performed in Figure 5a-b was correct.

On the other hand, the bulk always retained duplex stabilizing conditions ( $FRET > 0.8$ ) for pH down to  $\sim 4.3$ . An acidification of this magnitude is however not observed for buffered solutions at 1 bar  $pCO_2$ , which normally remain in a more neutral regime<sup>15,16</sup>. Therefore, the bulk is expected to retain annealing conditions also at the higher

temperatures of the experiments shown in Figure 3d, 4a-c, 4d. In fact, its duplex-stabilizing conditions are confirmed by the FRET measurements in Figure 3d and by the SYBR Green signal in Figure 4a-c, which only fluoresces in the presence of dsDNA.

According to [Sigma-Aldrich](#), the pH of a Tris solution decreases of 0.25 pH units per 10 °C. We also measured that 1 bar of pCO<sub>2</sub> lead to a decrease in pH of 1.2 units (Figure 2a). The QIAGEN PCR Master Mix (which is buffered by 10 mM Tris) has an initial pH of 8.2. Summing the acidification induced by CO<sub>2</sub> and the temperature dependence of Tris, we obtain a pH of 6.0 at 67 °C and 1 bar pCO<sub>2</sub>. At a pH of 6, a 100 % DNA duplex fraction in the bulk is expected (Figure S5.4, black lines).

## 6. Finite Element Simulation of DNA accumulation at the heated gas-water interfaces

We simulated our dew chamber using the software COMSOL Multiphysics®: an evaporating bulk and dew in a thermal gradient. The capillary flow, the convection and transport of solved DNA molecules were simulated. The simulated geometry (3D) was identical to our dew chamber (5 mm x 10 mm x 250 µm, x y z respectively). The bottom 2/3 of the chamber were filled with liquid and the top 1/3 contained air and a single dew droplet. The shape of the meniscuses of the dew were determined experimentally by imaging the dew chamber laterally (y-z plane) and measuring the contact angles of the dew droplet at the cold (Teflon) and warm (sapphire) sides (Figure S6a). The materials at the sides of the chamber (Teflon and sapphire) and the temperatures determined the contact angle of water on that surface. The same contact angles for the bulk (Figure S6b) have then been assumed. The shape of the dew and bulk in the x-y plane was also identical to what observed experimentally (Figure 3).

The temperature profile within the chamber was calculated through solving the partial differential equations for transient heat transfer, given the temperatures at the warm and cold sides (60 °C and 43°C respectively), while insulating the top and the bottom of the chamber. The temperature profile is shown in Figure S6c. Evaporative cooling was implemented by adding a boundary heat source at the air-water interface:  $Q = H_{\text{vapor}} \cdot D_{\text{vapor}} \cdot \nabla c$  where  $H$  is the latent heat of vapor,  $D$  its diffusion coefficient, and  $c$  its concentration. The concentration profile of water vapor in the air was simulated by using a drift-transport diffusion equation:

$$\frac{\partial c}{\partial t} = \left( \frac{\partial^2 c}{\partial x^2} + \frac{\partial^2 c}{\partial y^2} \right) - u \frac{\partial c}{\partial x} - v \frac{\partial c}{\partial y} \quad (22)$$

As a boundary condition, the vapor concentration was fixed to saturation pressure at the air-water interface. The value of vapor concentration at the top of the chamber was a priori unknown, we therefore calculated this value experimentally by measuring the droplet evaporation rates (as discussed later).

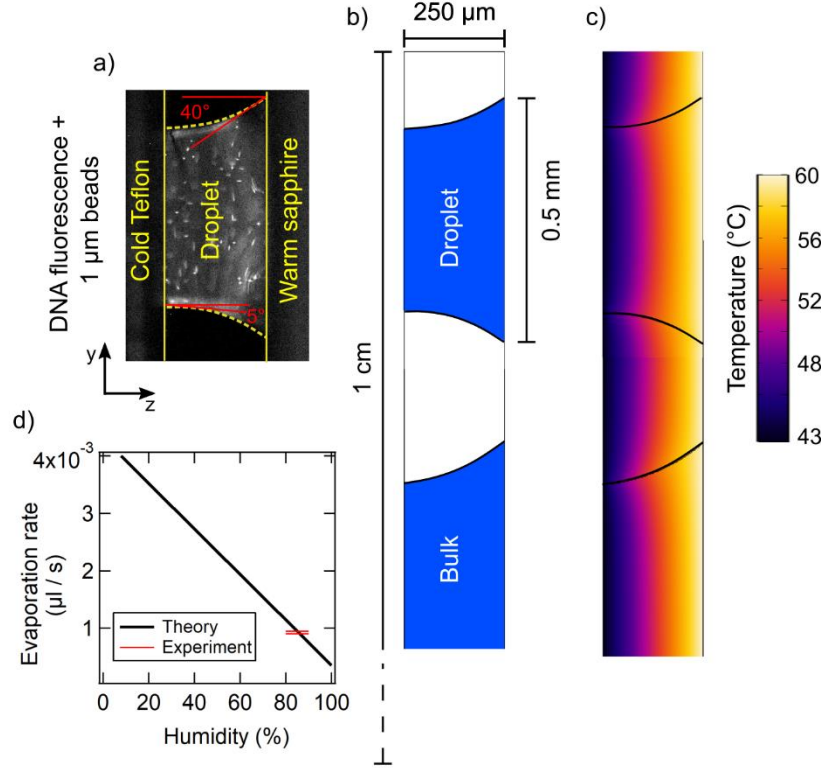


**Figure S6. Measurement of droplet geometry and implementation of the dew chamber for simulation.** a) Experimental picture used to obtain the lateral geometry of the dew droplets and the contact angles (red lines). The image was obtained by fluorescence microscopy, using FAM-labeled DNA (5 μM) and FAM-labeled beads 1 μm-sized. b) Geometry used in the simulation (y-z plane). c) Temperature gradient in our dew chamber (60 °C hot and 43 °C cold) calculated by finite element simulation. d) Evaporation rate in function of humidity. Comparing theory (black line) and experiments (red brackets) allowed us to deduce a humidity in the range of 80-90 % in our dew chamber.

As a result of the horizontal temperature gradient, the evaporation rate at the interface was stronger at the hot side than the cold side. Throughout the evaporation process, the interface maintained its geometrical shape, thus shrinking vertically downwards along the y axis. To compensate for the excess loss of water molecules at the warmer side of the interface, a capillary flow arose (the so-called coffee-ring effect<sup>17</sup>). We derived an expression for the velocity profile at the gas-water interface based on conservation of mass:

$$\vec{v} = \frac{-\rho}{M} (\vec{J} \cdot \vec{n}) \cdot \vec{n} - \Phi \vec{\tau}, \Phi_{\tau} = \frac{\Phi}{\int |\vec{\tau}| \cdot dS} \quad (23)$$

Where  $\rho$  is the density of water,  $J$  is the gradient of vapor concentration,  $n$  is the surface normal vector,  $\Phi$  is the total evaporation rate, and  $\tau$  is the vector along which the volume shrinks. The parameters  $\Phi$  and  $\tau$  were obtained experimentally. For the bulk interface, the volume shrank vertically along the y-axis, therefore  $\tau = \hat{e}_y$ . The capillary bridge shrank radially inwards, and therefore  $\tau = \hat{e}_x + \hat{e}_z$  was a good approximation. The total evaporation rate  $\Phi$  was obtained by experimentally investigating the change in volume of the droplet. The change in volume was linear in time, which is in good agreement with other research<sup>18</sup>. The experimental results were then compared to those obtained with a finite element simulation, and found these to be compatible with a humidity value at the top of the chamber in the range between 80-90%. Data are shown in Figure S6d.

The capillary and convective flow profiles were obtained by numerically solving the Navier-Stokes equations for incompressible fluids. The convection flow was modeled by including the gravitation volume force as



the external force on the fluid. The capillary flow was implemented as a velocity profile at the gas-water interface. The accumulation of DNA was simulated using equation (22), where the velocities  $u$  and  $v$  were given by the sum of the liquid velocity and thermophoretic velocity:  $D_T \cdot \nabla T$ , where  $D_T$  is the thermophoretic mobility of DNA. The thermophoretic speeds were much slower than that of the liquid, therefore making the impact of thermophoresis on our experiments relatively weak. Diffusion, on the other hand, proved to be of great importance to our work. In particular, the length dependence of the diffusion coefficient of DNA explains why we observed a stronger accumulation of longer DNA strands than shorter ones. Moreover, our simulations showed a significantly greater accumulation at the bulk interface than in the droplet. This effect was attributed to the superposing of convective and capillary flows in the bulk. This effectively created a long range divergent flow, which had a large reservoir of molecules to accumulate. This means that a longer chamber could accumulate DNA molecules stronger.

All simulations were performed for a total time of 200 s, which was a reasonable length to assume the simulation to have reached a steady state. However, also in our dew chamber the lifetime of a droplet (in the range between 10 and 100 seconds) was usually shorter than the time needed to reach a complete steady state for DNA accumulation. After tens of seconds, a dew droplet was seen coalescing back in the bulk or completely drying on the hot sapphire. The simulation is given in the attached file "simulation\_dew.mph".

To experimentally validate the results of the simulation, we performed dual-channel fluorescence imaging using differentially labeled DNA molecules of different lengths: FAM-labeled 8 nt ssDNA, ROX-labeled 51 nt ssDNA. The two strands were added at a final concentration of 1  $\mu\text{M}$  in a solution of 10 mM  $\text{MgCl}_2$ , 10 mM Tris, at pH 7. The solution was then inserted into the thermal trap, and the same temperature gradient as the simulation of Figure 3 was applied ( $\Delta T = 17^\circ\text{C}$ : hot side  $60^\circ\text{C}$ , cold side  $43^\circ\text{C}$ ). For matter of simplicity, the atmosphere has not been enriched with  $\text{CO}_2$  (DNA convection and accumulation are independent of that anyway). The microscopy images have been obtained using the same imaging protocol shown in supplementary section 4, taking two consecutive images (FAM channel and ROX channel, 50 ms exposure time each), every 1 second. Results are shown in the following figure.

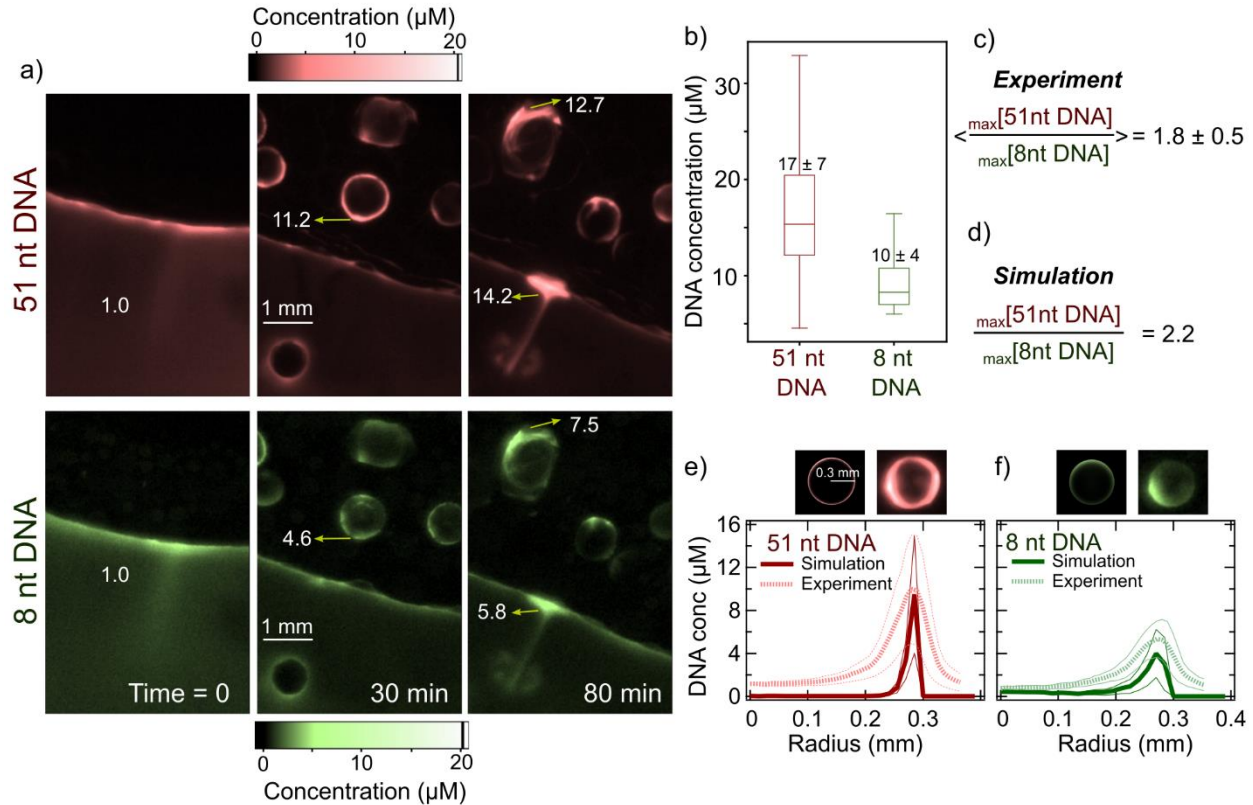


**Figure S6.2. Longer DNA strands accumulate stronger at the gas-water interfaces.** a) Dual-channel fluorescence images showing DNA accumulation in the bulk and fog, for a 51 nt DNA (ROX-labeled, top) and an 8 nt DNA (FAM-labeled, bottom), at different times. The numbers in the images correspond to DNA concentration. The 51 nt DNA accumulated much stronger than the 8 nt one. b) Quantification of DNA accumulation at the dew's gas-water interface over the course of the experiment (~5000 frames, total duration ~ 1.5 hours). The average max fold increase in the concentration of 51 nt DNA over the 8 nt DNA results to be  $1.8 \pm 0.5$  in the experiment (c) ( $n = 1513$ ), and 2.2 in the simulation (d) ( $n=1$ ). e) DNA concentration as a function of the droplet radius (circular average). Experiment (dashed lines) has been compared with the simulation (thick line). Thinner lines indicate the standard deviation. Qualitative pictures of the droplets of interest are shown on top (left = simulation, right = experiment). f) Same as (e) but for the 8nt DNA.

As shown in Figure S6.2a, in the heated rock pore DNA accumulates at the gas-water interface of the bulk and of the dew. The longer DNA (51 nt) accumulates stronger than the shorter one (8 nt). The average concentration of the 51 nt DNA at the dew's gas-water interface is  $17 \pm 7 \mu\text{M}$ , against  $10 \pm 4 \mu\text{M}$  for the 8mer ( $n = 1513$ ) (Figure S6.2b). At the brightest spot (i.e. most concentrated, indicated as "max") of the dew droplet, the concentration ratio between the 51 nt and the 8 nt resulted to be  $1.8 \pm 0.5$  for the experiment ( $n = 1513$ ) and 2.2 for the simulation ( $n = 1$ ) (Figure S6.2c-d). The experimental and simulated DNA concentration profiles of the dew droplet (radially averaged) show an impressive agreement (Figure S6.2e-f). However, the simulated profile looks slightly narrower and sharper than the experimental one. This is probably attributed to the inevitable diffraction of light through the lenses and the optical path of the microscope. It is important to note that only one single droplet was selected for the profile analysis. In the experiment, however, many droplets of different size form over time, which pick up variable amounts of dried DNA. The final maximum DNA concentration at the dew's gas-water interface is in fact very variable, as we showed in Figure S6.2b.

## 7. Sequencing of the longer DNA replication products

We sequenced the DNA products of the replication reaction in the CO<sub>2</sub> dew chamber shown in Figure 4d (6<sup>th</sup> lane), where two DNA templates of different lengths (47 bp and 77 bp) were replicated. Apart from the replication of the templates, also the formation of unexpected products has been observed. We sequenced them using the MinION Oxford Nanopore sequencing technology. The detailed protocol for DNA purification and preparation for sequencing is written in the material and methods. The sequencing procedure yielded 2856 reads. The length distribution of the reads is shown in Figure S7.1

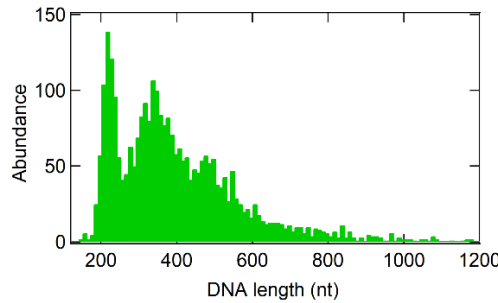


**Figure S7.1: Length distribution of the reads generated by Nanopore sequencing.**

The Levenshtein string distance<sup>19</sup> has been used to measure the distance between the reads and the templates and primers. It is defined as:

$$Lev_{a,b}(i,j) = \begin{cases} \max(i,j) & \text{if } \min(i,j) = 0, \\ \min \begin{cases} Lev_{a,b}(i-1,j) + 1 \\ Lev_{a,b}(i,j-1) + 1 \\ Lev_{a,b}(i-1,j-1) + 1_{(a_i \neq b_j)} \end{cases} & \text{otherwise.} \end{cases} \quad (24)$$

where  $Lev_{a,b}(i,j)$  is the distance between the first  $i$  characters of the string  $a$  and the first  $j$  characters of the string  $b$ .  $1_{(a \neq b)}$  is the indicator function, which equals 0 when  $a=b$ , and equals 1 otherwise. The result is a matrix of size  $a+1 \times b+1$  where the entries of the matrix indicate how many steps (character insertion, deletion or substitution) are required to convert one string into the other. The last cell of the matrix therefore indicates the distance between the strings  $a$  and  $b$ , i.e. the total number of steps that are necessary to completely convert  $a$  into  $b$  (or *vice versa*).

We calculated the Levenshtein distance for a specific sequence  $a$  (template or primer) mapped on the read  $b$ , looping over all possible substrings of length  $a$  of the read. This yielded a Levenshtein distance for the sequence in function of the read position, which was then converted into a probability in the following way:

$$Probability(a) = 1 - \frac{Lev_{distance}(a, b_{substring})}{Length(a)} \quad (25)$$

Some examples of the raw alignment data can be seen in Figure S7.2a-b. From the probability vs position plots we then reconstructed the sequence structure, as shown in Figure S7.2c-d.

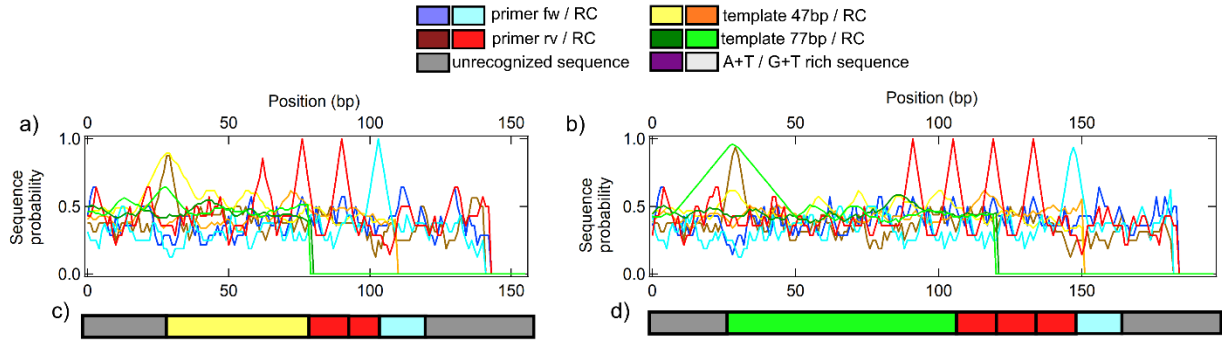


**Figure S7.2: Analysis and reconstruction method of the sequences created in the dew.** a-b) Raw data showing the probability of matching of every primer or template sequence as a function of the read position. A spike indicates the start of the match. c-d) Sequence reconstructed according to the plot shown above. RC = reverse complement.

Some sequences revealed to contain many repetitions of primers and templates (Figure S7.3a) attached one after the other, with a length distribution in the range between 150-300 nucleotides. These sequences correspond to the pink blob that can be seen in Figure 5a-b. Figure S7.3b shows the structure of the longer, AT rich sequences (the white pool of Figure 5a). They contain extended regions rich in As and Ts, and also eventually some primers and templates.

The whole analysis of the sequence alignments and reconstruction has been performed using LabVIEW.

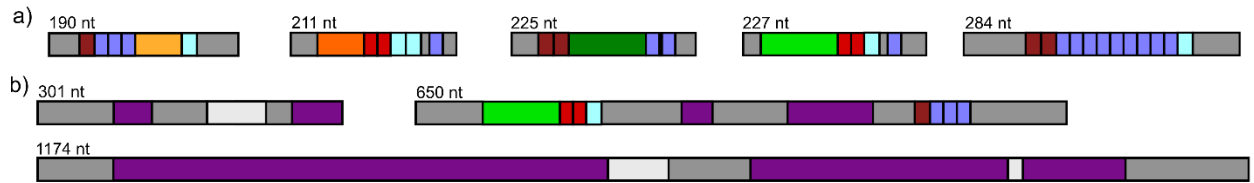


**Figure S7.3: The CO<sub>2</sub> dew creates sequences with repeated primer/template patterns and very long AT rich ones.** a) Examples of sequences that contain repetitive structures made of primers and templates. b) Long (300 - 1300 nt) DNA sequences that contain AT rich regions.

## 8. Modeling unspecific replication in the CO<sub>2</sub> dew droplets

In the experiments shown in Figure 5 we determined that the CO<sub>2</sub> dew droplets are able to replicate DNA and drive their evolution towards longer DNA sequences. Their sequence composition (indicated as AT:GC ratio) correlates with the denaturing conditions of the dew droplets. In particular, the long sequences that were replicated had an average duplex fraction (i.e. DNA FRET) of  $0.14 \pm 0.12$ .

We developed a probabilistic model to describe the replication and evolution of DNA sequences under the denaturing conditions of the CO<sub>2</sub> dew (acidic pH and low salts). The algorithm is shown in Figure S8.1.

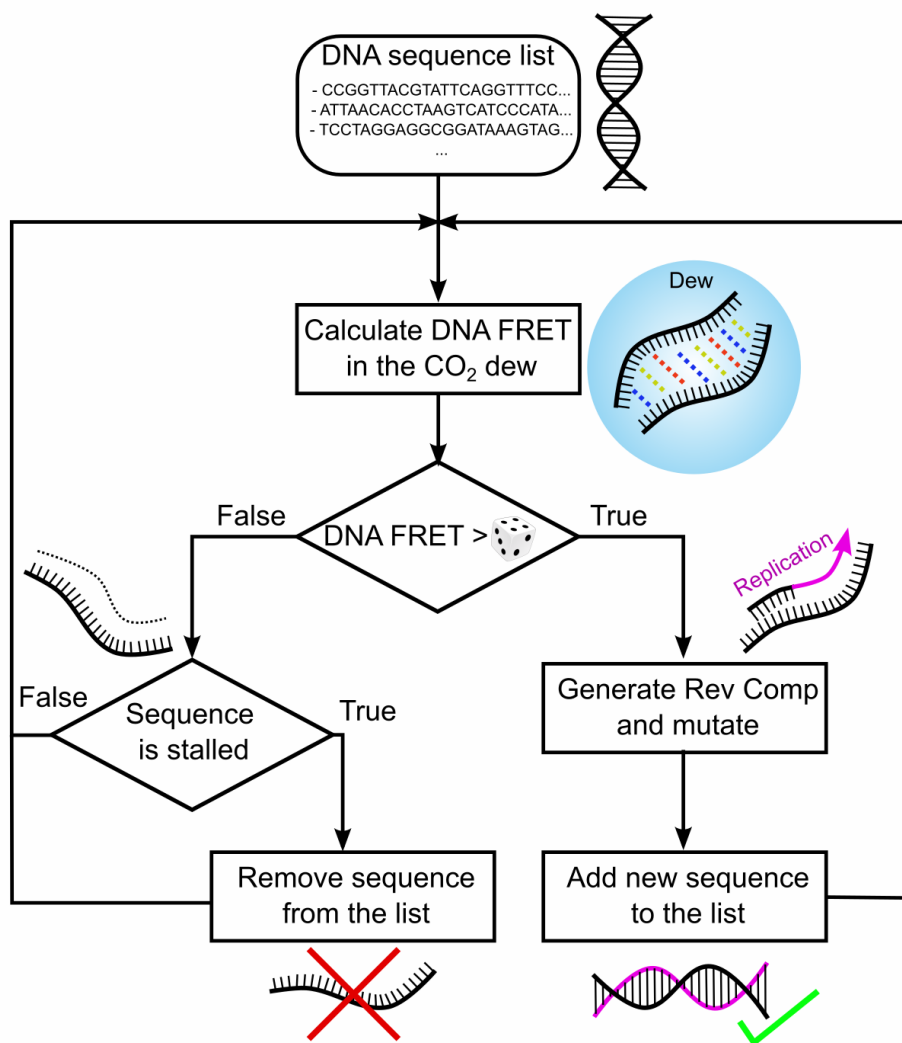


Figure S8.1: Algorithm of the stochastic replication model.

Every sequence in the pool has a probability of being replicated based on their duplex fraction, as indicated in Figure S8.2a (determined from the experiments,  $0.14 \pm 0.12$ ). This introduces a selection pressure, resulting in the preferential replication of sequences with intermediate stability ( $\text{FRET} \sim 0.14$ ). The sequences with a too high melting temperature ( $T_m$ ) do not melt, and therefore do not provide single strands to initiate the next templated polymerization cycle. The sequences with a too low  $T_m$  remain in the single-stranded form and do not bind a template that can then be elongated via polymerization. In both cases, such sequences would stall and die out.

When a replication step is initiated, the reverse complement (RC) of the sequence is created. Then, a modification of the RC sequence takes place: it can be elongated or shortened. The probability of being elongated ( $p$ ) vs being shortened ( $1-p$ ) has been screened in Figure 5a-b ( $p$  from high to low: 1.0, 0.9, 0.84, 0.8, 0.7, 0.6), and

yields results similar to the experiment for  $1.0 \geq p > 0.5$ . Experimentally, the insertion or deletion of nucleotides may occur via processes such as unspecific annealing, hairpin formation and other self-templating processes<sup>20</sup>. A similar principle has been applied in our simulation. An elongation step consists of the insertion of a random submer of random length (between 0 and 15 nt, chosen with uniform probability) at a random position in the sequence. A shortening step consists of the deletion of a random part of the sequence of random length (again, between 0 and 15 nt, chosen with uniform probabilities). Moreover, at each step of elongation or shortening, a mutation rate on the sequences of  $1e-4$  mutations/nt has been introduced (this number corresponds to the error rate of the *Taq* polymerase enzyme<sup>21</sup>). The process is completely stochastic and therefore excludes any specific sequence bias that could have possibly been introduced by the polymerase enzyme in our experiments.

The size of the sequence pool was maintained constant at ~3000. When the size of the sequence pool exceeded that number (because of replication), the sequences were removed according to their propensity of being replicated: the sequences that stalled during the previous cycles of replication, because their  $T_m$  was too high or too low, were removed. This step emulates the sequences that die out during the replication process.

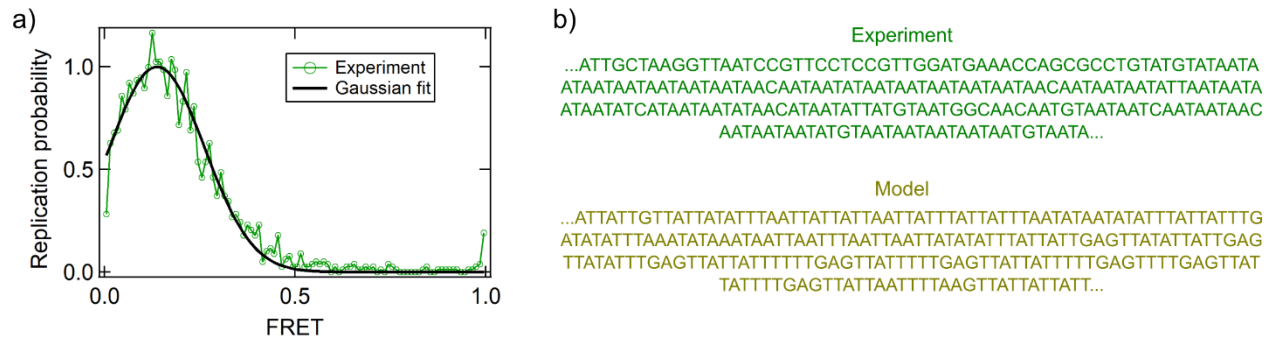


**Figure S8.2: Model for the replication of sequences in the CO<sub>2</sub> dew.** a) Replication probability as a function of DNA duplex stability (FRET). The highest replication probability occurs for FRET of  $0.14 \pm 0.12$ . Green data correspond to experimental data (Figure 5a), and they have been fitted with a Gaussian function (black line). b) Example of the sequences obtained in the experiment of DNA replication in the CO<sub>2</sub> dew (green) or using the replication model (yellow). Both sequences contain repeated AT rich motifs.

The simulation was run for about 100-150 steps, until the average sequence length distribution matched the reads observed experimentally in the CO<sub>2</sub> dew replication. A qualitative comparison is shown in Figure S8.2b and Figure 5. The sequences obtained by the simulation matched many features of the experiments. They were rich in A and T (A + T fraction > 80%), their submer composition showed a strong reduction in entropy and their final AT : GC ratio was determined by the denaturing conditions of the dew (with higher temperatures favoring sequences richer in GC). The model reproduced well what we observed experimentally. It provides a robust and enzyme-free confirmation of the general mechanism of how the CO<sub>2</sub> dew can drive the replication and evolution of DNA sequences.

The entropy of the sequences was calculated using the Shannon entropy (H), given a discrete variable  $X$  with possible outcomes  $x_1, \dots, x_n$ , that have probability  $P(x_1), \dots, P(x_n)$  to occur:

$$H(X) = - \sum_{i=1}^n P(x_i) \log P(x_i) \quad (26)$$

It was calculated over the submer counts shown in Figure 5c.  $P(x_i)$  corresponded to the normalized count (probability) of a specific submer ( $x_i$ ) in the whole set ( $n$ ) of submer combinations, with length  $X$ . In other words, the recurrence of each subsequence of given length was counted, and the probability of each submer was calculated. The entropy was then normalized on the random pool, in order to measure the relative change in entropy to the maximum possible entropy (which corresponds to the random pool).

## 9. List of attached files

supplementary\_movie\_1\_fluorescent\_droplets.avi  
supplementary\_movie\_2\_FRET\_and\_pH.avi  
supplementary\_movie\_3\_DNA\_replication.avi  
melting\_curve\_calculator.exe  
simulation\_file\_dew.mph  
source data for figures 2-5

## 10. References

1. Al-Hindi, M. & Azizi, F. Absorption and desorption of carbon dioxide in several water types. *Can. J. Chem. Eng.* **96**, 274–284 (2018).
2. Gillian M. Bond, \*,† *et al.* Development of Integrated System for Biomimetic CO<sub>2</sub> Sequestration Using the Enzyme Carbonic Anhydrase. (2001). doi:10.1021/EF000246P
3. Pocker, Y. & Bjorkquist, D. W. Stopped-flow studies of carbon dioxide hydration and bicarbonate dehydration in water and water-d<sub>2</sub>. Acid-base and metal ion catalysis. *J. Am. Chem. Soc.* **99**, 6537–6543 (1977).
4. Gordon, G. E. Chemistry of the Natural Atmosphere. Peter Warneck. Academic Press, San Diego, CA, 1988. xiv, 757 pp., illus. \$85. International Geophysics Series, vol. 41. *Science* **242**, 121–2 (1988).
5. Keil, L. M. R., Möller, F. M., Kieß, M., Kudella, P. W. & Mast, C. B. Proton gradients and pH oscillations emerge from heat flow at the microscale. *Nat. Commun.* **8**, 1897 (2017).
6. Greenwood, N. N. & Earnshaw, A. *Chemistry of the elements*. (Butterworth-Heinemann, 1997).
7. Soli, A. L. & Byrne, R. H. CO<sub>2</sub> system hydration and dehydration kinetics and the equilibrium CO<sub>2</sub>/H<sub>2</sub>CO<sub>3</sub> ratio in aqueous NaCl solution. *Mar. Chem.* **78**, 65–73 (2002).
8. Deegan, R. D. *et al.* Capillary flow as the cause of ring stains from dried liquid drops. *Nature* **389**, 827–829 (1997).
9. Kapanidis, A. N. *et al.* Fluorescence-aided molecule sorting: Analysis of structure and interactions by alternating-laser excitation of single molecules. *Proc. Natl. Acad. Sci.* **101**, 8936–8941 (2004).
10. Ianeselli, A., Mast, C. B. & Braun, D. Periodic Melting of Oligonucleotides by Oscillating Salt Concentrations Triggered by Microscale Water Cycles Inside Heated Rock Pores. *Angew. Chemie Int. Ed.* (2019). doi:10.1002/anie.201907909
11. Mast, C. B., Schink, S., Gerland, U. & Braun, D. Escalation of polymerization in a thermal gradient. *Proc. Natl. Acad. Sci. U. S. A.* **110**, 8030–5 (2013).
12. Whitaker, J. E., Haugland, R. P. & Prendergast, F. G. Spectral and photophysical studies of benzo[c]xanthene dyes: Dual emission pH sensors. *Anal. Biochem.* **194**, 330–344 (1991).
13. Mariani, A., Bonfio, C., Johnson, C. M. & Sutherland, J. D. pH-Driven RNA Strand Separation under Prebiotically Plausible Conditions. *Biochemistry* **57**, 6382–6386 (2018).
14. Peng, C., Crawshaw, J. P., Maitland, G. C., Martin Trusler, J. P. & Vega-Maza, D. The pH of CO<sub>2</sub>-saturated water at temperatures between 308 K and 423 K at pressures up to 15 MPa. *J. Supercrit. Fluids* **82**, 129–137 (2013).
15. Liu, Q. & Maroto-Valer, M. M. Investigation of the effect of brine composition and pH buffer on CO<sub>2</sub> -brine

- sequestration. *Energy Procedia* **4**, 4503–4507 (2011).
16. Holmes, J. D. *et al.* Buffering the Aqueous Phase pH in Water-in-CO<sub>2</sub> Microemulsions. *J. Phys. Chem. B* **103**, 5703–5711 (1999).
  17. Deegan, R. D. *et al.* Capillary flow as the cause of ring stains from dried liquid drops. *Nature* **389**, 827–829 (1997).
  18. Carrier, O. *et al.* Evaporation of water: Evaporation rate and collective effects. *J. Fluid Mech.* **798**, 774–786 (2016).
  19. Levenshtein, V. I., Levenshtein & I., V. Binary Codes Capable of Correcting Deletions, Insertions and Reversals. *SPhD* **10**, 707 (1966).
  20. Park, D., Ellington, A. D. & Jung, C. Selection of self-priming molecular replicators. *Nucleic Acids Res.* **47**, 2169–2176 (2019).
  21. Potapov, V. & Ong, J. L. Examining sources of error in PCR by single-molecule sequencing. *PLoS One* **12**, (2017).